https://doi.org/10.1016/j.ijmecsci.2022.108049

Dynamical modeling and parametric analysis of an electret-based wave energy converter

Yiqiang Fu*, Haihui Ruan*

Research Center for Fluid-Structure Interactions, Department of Mechanical Engineering, The Hong Kong Polytechnic University, Hung Hom, Kowloon, Hong Kong, China.

*Corresponding author. Email: haihui.ruan@polyu.edu.hk (H. Ruan); yiqiang.fu@polyu.edu.hk (Y. Fu).

Abstract

Carbon neutrality and the Internet of Underwater Things have injected new impetus into the development of wave energy converters (WECs) albeit most of WEC projects have ended in failure due to low cost-effectiveness. Hereupon we present the dynamical modeling and parametric analysis of a novel electret-based WEC that has a distinct power take-off system compared to the conventional ones and has exhibited high power density in our previous study. Linear wave theory and Morison equation are applied for wave field and forces, respectively. WEC motions parallel with incident waves are modeled, and the electrical subsystem of the generator is treated as a current source and a capacitor. With these simplifications, the governing equations of the nonlinear and non-smooth electromechanical system are obtained and then numerically solved using an event-driven algorithm. The new power take-off system is experimentally validated. We find that the power output varies nonlinearly with wave parameters under regular wave excitation but linearly under irregular ones, and that superharmonic resonance can significantly enhance energy conversion performance at relatively low frequencies, based on which the optimum parameters are obtained. A peak average power of around 2 mW (at a matched load resistance) is generated from each generator encapsulated in the WEC of a diameter of 15 cm. The findings shed light on the characteristics of electret-based WECs and provide support for the development of wave energy farm; moreover, the methodologies of modeling and analysis can be extended to the design and optimization of the scaleups of the proposed electret-based WEC.

Keywords:

Wave energy converter; Electret-based energy harvester; Morison equation; Nonlinear dynamics; Superharmonic resonance.

1. Introduction

Wave energy is seen as the largest untapped renewable energy on planet earth. It is estimated that the potential exploitable wave energy resources worldwide is around 2 TW [1]—around three quarters of the world electricity consumption in 2020 [2]. Study of wave energy converters (WECs) was first stimulated by the emerging oil crisis of the 1970s [3,4], and new impetus to its development have been injected by carbon neutrality and the Internet of Underwater Things (IoUT). Despite the numerous devices proposed, the development of a WEC competent for large-scale deployments, e.g., wave farms, is still in vain. One of the main reasons behind is the lack of cost-effectiveness. Indeed, the device cost of some popular commercial WECs, such as Pelamis [5] and Wave Dragon [6,7], ranged from million to tens of million US dollars, giving rise to high price per watt ($/W), and thus most ended in failure. Therefore, novel cost-effective WEC is in great need.

In comparison with conventional WECs that employ heavy and costly rare-earth magnets to achieve electromagnetic induction for energy conversion, WECs based on triboelectrification and/or electrostatic induction have the merits of high power density, low fabrication cost, and lightweight structures [8,9], and thus they are regarded as promising alternatives. Moreover, preference is given to electret-based or electrostatic WECs, because the frictional contact for triboelectrification [10] can greatly reduce the durability or lifetime [11], and corona-treated (one of the most common electret fabrication techniques [12]) polymers can have higher surface charge density and more uniform charge distribution than that of tribo-charged ones [13]. Nonetheless, efficient electret-based WECs are still in need despite the various relevant generators [14–17] proposed, such as rotational electret-based generators with low profile using flexible print circuit board technology [14] and long-term stable hydroxyapatite ceramic electrets [16]. Although some rotary generators are demonstrated to have high energy conversion efficiency up to 56% [17], the driving rotation speed is too high (750 rpm) and deviates from practical applications. Besides, some triboelectric WECs structured similar to sleigh bells [18,19] are proposed to harvest energy from random-directional waves, and origami structures have been used to improve contact-electrification [19]. However, these studies are mainly carried out from the perspectives of materials. To fully unveil the characteristics of a WEC based on triboelectrification and/or electrostatic induction, dynamic analysis is indispensable.

The power take-off (PTO) systems of the conventional WECs are often hydraulic [20,21], pneumatic [22,23], or electromagnetic (linear generators) [24,25]. Apparently, these conventional PTOs are usually quite complex but have often been simplified to spring-damper systems in many studies [26–28]. Nonlinearities have been included, for better representations, in the form of quadratic dampers [29]

considering that the oil flow rate in hydraulic PTOs is proportional to pressure difference squared, nonlinear end-stop [30] for avoiding damage under extreme wave loadings, and nonlinear snap-through [31] for improving energy conversion performance. Nevertheless, these models only interpret the dynamics of the mechanical subsystems of PTOs, and the power generation is often approximated by the product of damping coefficient and velocity squared [32]. Dynamics of the electrical subsystem, however, is rarely modeled and studied.

In this work, we focus on the dynamical modeling and parametric analysis of an electret-based WEC which is distinct from the conventional ones in terms of PTO and has been demonstrated to have high power density and low cost, outperforming most of the WECs based on electrostatic induction and/or triboelectrification, in our previous study [33]. Its overall structure is a tethered spherical buoy that encapsulates electret-based rotational generators as PTO. The simplified structure allows a detailed analysis of both mechanical and electrical systems, which is indispensable for WECs to be practically used. It is noted that the dynamics of a tethered buoy subject to incident waves has been extensively studied both theoretically and experimentally [34–36], and that particular attention has been paid to the Mathieu-type instabilities (parametrically excited motions) [27,36] which arise from time-varying stiffness coefficients for restoring forces or moments. Generally, such motion instabilities are unfavourable to WECs as they tend to be associated with a decrease of the productive modes of motion (e.g., heave for most of point absorbers) [27] as revealed in our preliminary experimental and analytical studies [33].

When the wave height is small compared to the wavelength (in deep water) or the still water depth (in shallow water), linear (Airy) wave theory [37,38] based on irrotational flow of an inviscid and incompressible fluid can be applied for the wave field. Moreover, despite the inviscid assumption, if the WEC is relatively small compared to wave amplitude, viscous loss is considered relevant and should be included in modeling [39], e.g., by involving an additional linear damping or a quadratic drag term from the Morison equation [40]. Indeed, at intermediate Keulegan–Carpenter (KC) numbers [41], both viscous and inertial effects are important, and Morison's equation [40], which includes an inertia force and a drag force related to water particle acceleration and velocity, respectively, can be used to account for the total wave force acting on the structure. Obviously, the non-smooth drag term in Morison's equation complicates the numerical integration and thus has been linearized using Fourier series in some studies [34,36]. However, such approximation may not be adequate to interpret some nonlinear dynamic phenomena that the system may exhibit. It is noteworthy that both the mechanical and electrical subsystems of the WEC proposed in this work are non-smooth, but no smooth approximation will be applied, and the non-smooth dynamics will be coped with event-driven algorithms in numerical integration.

The outline of the rest of this paper is as follows: Section 2 introduces the designs and working mechanisms of the proposed electret-based rotational generators (i.e., the PTO) and WEC. Dynamical modeling is presented in Section 3, where Airy wave theory and Morison equation are applied for wave field and forces, respectively, surge and heave motions of the WEC are considered only, the electromechanical system of the electret-based rotation generator is established, and the coupled governing equations of the WEC system are derived. Section 4 discusses the results obtained, where the numerical implementation is first introduced, the electret-based generator is then experimentally validated, and parametric studies on the dynamics of the system are finally carried out under both regular (mainly) and irregular (secondarily) wave excitations. The final section concludes this research by giving an overview of the investigation and a summary of numerical results.

2. Designs and working mechanisms

In this section, the unique designs of both the electret-based rotational generator and WEC will be introduced first, and then their working mechanisms interpreted to illustrate how wave energy is converted into electricity. The key materials and components used in a WEC prototype will be highlighted in this section, and a more detailed description and demonstration of the WEC can be found in [33].

2.1. Designs

The schematic diagrams of the electret-based WEC are shown in Fig. 1 (more experimental details can be found in [33]). The electret-based rotational generator or the PTO is composed by a stator that has two comb-like electrodes (1 and 2) and a rotator (12 cm in diameter) that has electret sectors in a pattern similar to that of electrodes, as shown in Fig. 1(a). Note that the number of the comb teeth of each electrode equals that of the electret sectors (i.e., 15 in the schematic diagram) and is one of the key parameters to be studied herein. The exploded view and the assembled state of the generator are presented in Fig. 1(b) and (c), respectively. The stator and the rotator sit closely on the shaft (via bearings and flange, respectively) with electrodes facing electrets and are separated by ceramic balls with a gap around 0.3 mm. The stator has four keys at its periphery in order to couple with and thus maintain stationary to the shell, leaving only the rotator rotating with the shaft.

An exploded view of the WEC is shown in Fig. 1(d). The generator module is encapsulated in a hemispherical shell, and two (identical) such hemispheres form a complete WEC (which thus has two generators). It is worth mentioning that more generator modules can be accommodated, and the encapsulation of a serial assembly of generators with stepped diameters is closer to our conception and is more efficient for practical applications. Other principal components include torsional springs for restoring torque, a winch for both winding tether and coupling hemispheres, and gaskets and lids for waterproofing.

The assembled WEC is shown in Fig. 1(e) and has a diameter of 15 cm. Note that such a small dimension is for a proof of concept only, and scaleup devices are certainly more favourable for practical applications. As most of the components can be made of plastics, we expect that the scaleup devices can be much more cost-effective than the WECs previously attempted.

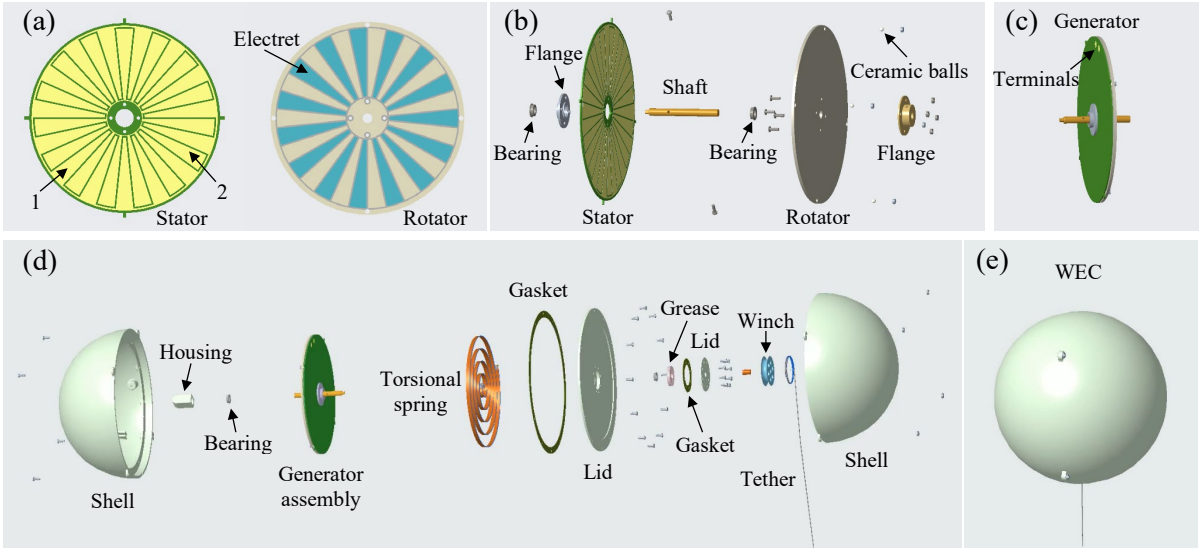

Fig. 1 Schematic diagrams of the proposed WEC. (a) Schematic diagrams of the stator and rotator of the electret-based rotational generator. The two groups of electrodes are patterned in a comb-like structure. (b) Exploded view of the generator (only key components are annotated). (c) Generator assembly. Both the rotator and the stator sit on the shaft, but only the former follows shaft's rotation. (d) Exploded view of the WEC (only a half is shown due to symmetry). Each half encapsulates one generator module. (e) WEC assembly with a diameter of 15cm.

2.2. Working mechanisms

Negative corona discharge treatment of a PTFE film (a dielectric material that has excellent charge retention ability) converts it into an electret that has a quasi-permanent state of electric polarization and generates electric fields [42]. The negatively charged electret in the proposed generator plays a role (electrostatic induction) similar to that of the magnet (electromagnetic induction) in an electromagnetic generator. The working mechanism of the electret-based rotational generator is depicted in Fig. 2(a). As the gap between the electret and the comb-like electrodes is small, the same number of positive charges can be induced in the latter (electrode 1 or 2 or their sum). Although the total number of induced charges remains constant, their distribution varies against the rotation of the rotator, giving rise to the variation of potential difference between electrodes and thus the electron or current flow through the load resistance R. For example, the current flows from electrodes 1 to 2 when the electret moves in the same direction, and vice versa, as shown in Fig. 2(a).

The WEC is taut-moored by a single tether with one end anchored into the seabed or the bottom of a water wave channel and the other end winding up on the winch, as shown in Fig. 2(b). When the WEC is elevated or sunk by waves, the mooring tether winds off or on the winch, resulting in forward or backward rotation of generators (or rotators), which then accomplishes the energy conversion from wave energy into electricity.

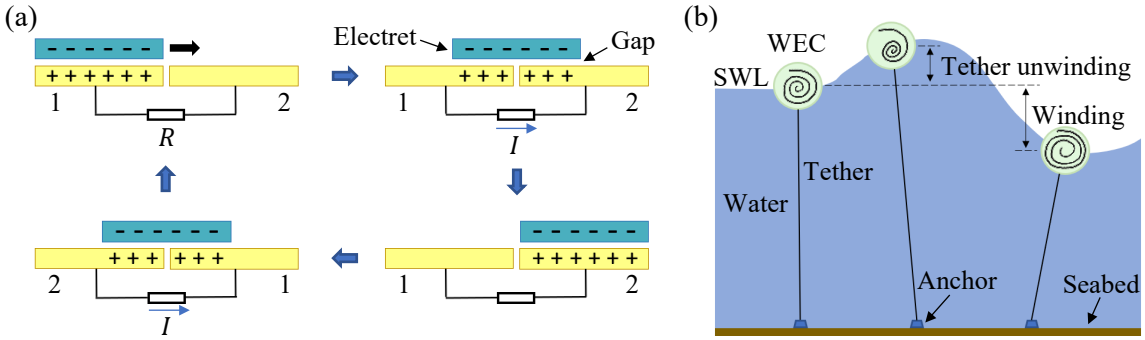

Fig. 2 Schematic diagrams of the working mechanisms of (a) the electret-based rotational generator and (b) the WEC (SWL represents still water line). The generator relies on electrostatic induction for energy conversion. The spirals represent torsional springs in different states, namely initially tightened (taut-moored), further tightened due to wave crests, and relaxed due to wave troughs, from left to right.

3. Dynamical modeling

This section presents the dynamical modeling of the electret-based rotational generator and WEC. Linear wave theory and Morison's equation will be used for modeling water waves and their forces on the WEC, based on which the governing equations of the oscillation of the WEC will be derived. With the equations of WEC motion, the electromechanical model of the generator will be given, and the detailed expressions of the governing equations of the coupled system are given in Appendix.

3.1. Progressive water wave

A progressive water wave can be represented by a sum of cosines [43,44] and written as:

$$w(x,t) = \sum_{i=1}^{N} A_i \cos(\Omega_i t - k_i x) \tag{1}$$

where A_i and k_i are the wave amplitudes and numbers, Ω_i the wave frequency, and x the horizontal displacement or surge of the WEC. For the case of sinusoidal waves involving only the first harmonic ($N = 1$), the subscripts of wave parameters are omitted in the following context. This is the main case to be studied in the following sections; the case of irregular waves will be briefly discussed thereafter. Following

the derivations described in [43,44], the horizontal and vertical velocities of a water wave travelling in a channel are given by:

$$u(x,z,t) = A\Omega\frac{\cosh[k(z+h)]}{\sinh(kh)}\cos(\Omega t - kx) \tag{2}$$

$$v(x,z,t) = -A\Omega\frac{\sinh[k(z+h)]}{\sinh(kh)}\sin(\Omega t - kx) \tag{3}$$

where z is the vertical displacement or heave of the WEC and equals the height of the WEC with respect to the still water line (SWL), and h is the depth of the water. The schematic diagram of the oscillation of the WEC in water waves is shown in Fig. 3(a), where the WEC initially rests on the SWL and is half submerged. The tether is assumed to be massless and unstretchable and is in tension regardless of WEC's motion.

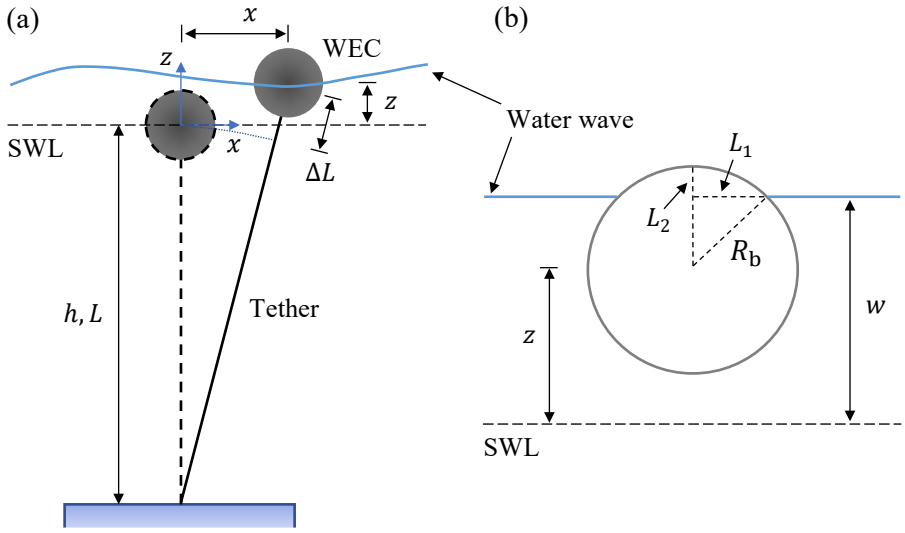

Fig. 3 Schematic diagrams of (a) the oscillation of the WEC in water waves and (b) the geometric relations. The WEC is taut-moored with its equilibrium lain on the SWL. Only the motions parallel with the incident waves are considered. For simplicity, the water wave line across the WEC is assumed uniform and horizontal.

3.2. Wave forces

The wave forces exerted on a floating structure can be categorized into two types, namely the inertia force, which accounts for the inertia of the displaced water and the neighboring water around the structure, and the hydrodynamic drag force that arises from surface shear, pressure gradients, and wake formation

[36]. The total force can be described by Morison's equation often employed to deal with structural vibration excited by waves [45], which is given by:

$$F_{\text{Morison}} = \rho V_{\text{s}} \dot{v}_{\text{f}} + \rho C_{\text{a}} V_{\text{s}} (\dot{v}_{\text{f}} - \dot{v}_{\text{s}}) + \frac{1}{2} \rho C_{\text{d}} A_{\text{p}} (v_{\text{f}} - v_{\text{s}}) |v_{\text{f}} - v_{\text{s}}| \tag{4}$$

where ρ is the density of water, V_{s} the submerged volume, C_{a} the added mass coefficient, C_{d} the drag coefficient, A_{p} the projected area in the flow direction, v_{f} and v_{s} the velocities of the water flow and the structure, respectively, and an over-dot denotes a partial derivative with respect to time t.

For the spherical WEC proposed herein, the components of the wave forces in the horizontal and vertical directions, as shown in Fig. 3(a), can be expressed as:

$$F_{\text{M}x} = \rho V_{\text{s}} (C_{\text{m}} \dot{u} - C_{\text{a}} \ddot{x}) + \frac{1}{2} \rho C_{\text{d}} A_{\text{p}x} (u - \dot{x}) |u - \dot{x}| \tag{5}$$

$$F_{\text{M}z} = \rho V_{\text{s}} (C_{\text{m}} \dot{v} - C_{\text{a}} \ddot{z}) + \frac{1}{2} \rho C_{\text{d}} A_{\text{p}z} (v - \dot{z}) |v - \dot{z}| \tag{6}$$

where C_{m} is the inertial coefficient and $C_{\text{m}} = 1 + C_{\text{a}}$, $A_{\text{p}x}$ and $A_{\text{p}z}$ are the projected areas of the submerged volume in the horizontal and vertical directions, respectively, and C_{a} equals 0.5 [36,46]. Assuming that the wave height across the WEC is even and according to the geometric relations shown in Fig. 3(b), the submerged volume V_{s} and the projected areas $A_{\text{p}x}$ and $A_{\text{p}z}$ can be obtained as follows:

$$V_{\text{s}} = \begin{cases} \frac{\pi}{3}\left(4R_{\text{b}}^3 - 3R_{\text{b}}L_2^2 + L_2^3\right), & -R_{\text{b}} < z - w \le 0 \\ \frac{\pi}{3} L_2^2 (3R_{\text{b}} - L_2), & 0 < z - w < R_{\text{b}} \end{cases} \tag{7}$$

$$A_{\text{p}x} = \begin{cases} L_1(R_{\text{b}} - L_2) + R_{\text{b}}^2 \left[\pi - \cos^{-1}\left(\frac{R_{\text{b}} - L_2}{R_{\text{b}}}\right)\right], & -R_{\text{b}} < z - w \le 0 \\ R_{\text{b}}^2 \cos^{-1}\left(\frac{R_{\text{b}} - L_2}{R_{\text{b}}}\right) - L_1(R_{\text{b}} - L_2), & 0 < z - w < R_{\text{b}} \end{cases} \tag{8}$$

$$A_{\text{p}z} = \begin{cases} \pi R_{\text{b}}^2, & -R_{\text{b}} < z - w \le 0 \\ \pi L_1^2, & 0 < z - w < R_{\text{b}} \end{cases} \tag{9}$$

where R_{b} is the radius of the WEC, and L_1 and L_2 are the radius and height of the dome above the waterline, respectively, given by:

$$L_1 = \sqrt{R_\mathrm{b}^2 - (z-w)^2} \tag{10}$$

$$L_2 = R_\mathrm{b} - |z-w| \tag{11}$$

3.3. Vibration of the WEC

Assuming that the rotations (roll, pitch, and yaw) of the WEC are negligible, a stable vibration (without transverse instability) of the WEC under sinusoidal wave excitation will only involve two degrees of freedom, i.e., surge and heave (x and z). The forces applied on the WEC include wave forces, net buoyance force, and tether tension force. Based on Newton's second law of motion, the governing equations for the vibrations of the WEC in surge and heave are written as:

$$m_\mathrm{b}\ddot{x} = F_{\mathrm{M}x} - F_{\mathrm{t}x} \tag{12}$$

$$m_\mathrm{b}\ddot{z} = F_{\mathrm{M}z} - F_{\mathrm{t}z} + F_\mathrm{b} \tag{13}$$

where m_b is the mass of the WEC, F_b is the net buoyancy force, and $F_{\mathrm{t}x}$ and $F_{\mathrm{t}z}$ are the components of the tether tension force in surge and heave, respectively, and they are expressed as:

$$F_\mathrm{b} = \rho V_\mathrm{s}\mathrm{g} - m_\mathrm{b}\mathrm{g} \tag{14}$$

$$F_{\mathrm{t}x} = F_\mathrm{t}\sin\alpha \tag{15}$$

$$F_{\mathrm{t}z} = F_\mathrm{t}\cos\alpha \tag{16}$$

where F_t is the total tether tension force and α is the angle between the tether and the vertical axis, and $\sin\alpha = x/\sqrt{(L+z)^2 + x^2}$ and $\cos\alpha = (L+z)/\sqrt{(L+z)^2 + x^2}$.

3.4. Rotation of the generator

The tether tension force drives the generators into rotation which is confined by the restoring torque arisen from the deformation of torsion springs. Since generators operate at low speeds, we neglect the vibrations caused by the elastic responses of the shaft and rotators and treat them as rigid bodies. Thus, the rotation of generators is governed by:

$$J\ddot{\theta} + c\dot{\theta} + k_\mathrm{s}\theta = \left(F_\mathrm{t} - F_\mathrm{p}\right)r_0 \tag{17}$$

where θ is the rotation angle, J the moment of inertia, c the damping coefficient which mainly comes from friction, k_s the combined stiffness of torsion springs, r_0 the radius of the winch, and F_p the pretension force which equals the net buoyancy force.

3.5. Electrical model

The electrical system of the electret-based rotational generator can be approximated by a current source and a capacitor, and the equivalent circuit is shown in Fig. 4, where I_s is the current source or the short-circuit current, C is the capacitance between the two comb-like electrodes on stators, and R is the load resistance connected to the generator or the WEC. It is noted that the output impedance of generators based on electrostatic induction and/or triboelectrification is usually much higher than the input impedance of conventional power management systems [47]. To circumvent the impedance mismatching problem, electronic [48], mechanical [49], plasma [50], or spark [51] switches can be utilized to reduce the output impedance of the generators. Since power management is not a focus of this paper, the connected circuit is simply represented by a resistive load R.

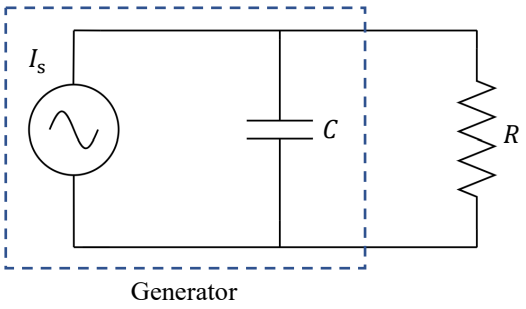

Fig. 4 Equivalent circuit of the electret-based rotational generator. The generator is equivalent to a current source and a capacitor.

Based on the development in Ref. [17], the governing equation of the electrical model of the generator or the WEC can be further written as:

$$RC\frac{dI}{dt} + I = I_s \tag{18}$$

$$I_s = \frac{1}{2}n\dot{\theta}(r_2^2 - r_1^2)\sigma\delta \tag{19}$$

$$\delta = \begin{cases} 1, & \dfrac{2m\pi}{n} \le \theta < \dfrac{(2m+1)\pi}{n} \\ -1, & \dfrac{(2m+1)\pi}{n} \le \theta \le \dfrac{2(m+1)\pi}{n} \end{cases}, m \in \mathbb{Z}^+ \tag{20}$$

where I is the current through the load resistance, n the number of teeth of each comb-like electrode or the number of the annular sectors of the electret, r_1 and r_2 the inner and outer radiuses of the electret, respectively, σ the surface charge density of the electret, and m a non-negative integer. Note that the change of rotation direction will reverse the sign of δ.

4. Results and discussion

A parametric study of the dynamics of the proposed WEC is performed in this section. The implementation of the numerical method will be introduced first. Then, an experimental validation of the electret-based generator will be demonstrated. The effects of some key parameters on the dynamic response and the energy conversion performance will be analyzed thereafter to reveal the dynamic behaviors and optimize the parameters.

4.1. Numerical implementation

Apparently, the dynamical system is non-smooth and the solution of the model demands the use of non-smooth event tracking methods in which the integration of the governing equations requires the detection of the non-smooth events, the solution of the non-smooth dynamics at these events with a reinitialization rule of the state, and the integration of the smooth dynamics between any two events [52].

Specifically, the non-smoothness exists in the relative velocities (Eqs. (5) and (6)) and heave (Eqs. (7) – (9) and (11)) between the WEC and waves, and in the rotation angle and speed of generators (Eqs. (19) and (20)). In other words, the wave forces, the submerged volume, the projected areas, and the short-circuit current are all non-smooth, and thus the numerical implementation is relatively tricky. Here, the MATLAB built-in function *events* and solver *ode15s* (which is used because the governing ordinary differential equation of the electrical system, i.e., Eq. (18), can be stiff) are used to handle with the non-smooth events and solve the smooth dynamics, respectively.

4.2. Experimental validation of the generator

Before encapsulating generators in the WEC, it is necessary to validate their functionality by standalone tests, i.e., driving the generator independently by a motor to have a glance at its performance. Under sinusoidal wave excitation, both the surge and heave of the WEC can be sinusoidal as well, and thus the rotation of generators can be sinusoidal swing. In fact, the swing of generators can always be regarded as a

superposition of sines or sinusoidal swings of different amplitudes, frequencies, and phases. Hence, a validation of the generator under sinusoidal swing can be sufficient.

The stator is a printed circuit board (PCB), as shown in Fig. 5(a), where the diameter and thickness of the substrate (FR4) is 120 mm and 1.5 mm, respectively, the comb-like electrodes are copper coatings with a thickness of 35 μm, and the electrode terminals are located at the back. The associated rotator is shown in Fig. 5(b), where the electret (50 μm thick, with an inner and an outer radii of 13.5 mm and 56 mm, respectively) is fabricated through negative corona charging [12] of PTFE films and is attached on the substrate (POM) in a pattern similar to that of the comb-like electrode. Note that the number of the slender annular sectors of the electret equals that of the teeth of each electrode. The assembled generator is tested with the setup shown in Fig. 5(c), where the rotator is driven by a closed-loop stepper motor, while the stator is kept stationary to the table.

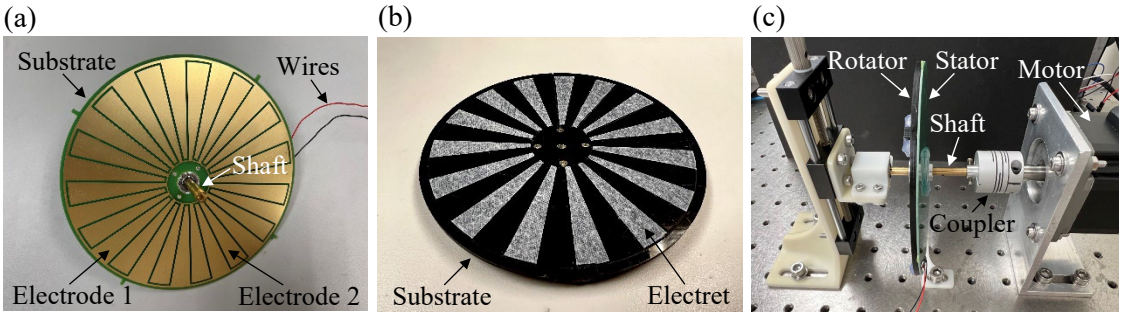

Fig. 5 Photos of the prototyped (a) stator (with the shaft installed), (b) rotator, and (c) generator and the test setup. The stator is fabricated using the PCB technology. The two terminals of the electrodes are located at the back. Corona-treated PTFE film serves as the electret and is patterned similar to the structure of the electrodes. Ceramic balls are used to maintain the air gap between rotator and stator.

The voltage across a load resistance of 80 MΩ is obtained (through Ohm's law using the current measured by a Keithley 6514 electrometer and a NI 9215 data acquisition board) at a driving frequency of 0.8 Hz under three different swing amplitudes of 23.04°, 57.60°, and 92.16°. The corresponding time histories in one excitation period (1.25 s) are shown in Fig. 6(a1 – c1), while those of the numerical simulation (C = 227 pF, σ = 36.16 μC/m^2) are presented in Fig. 6(a2 – c2) for comparison. It is noted that the overall agreement between experimental and numerical results is good, though differences exist in terms of waveform and amplitudes, which are caused by, respectively, the defective driving provided by the motor (especially at the swing amplitude of 23.04°), e.g., not perfect sinusoidal, and the error incurred by model parameters, e.g., less accurate evaluation of capacitance and surface charge density. In the time history, each peak corresponds to a travelling-across of one of the two electrodes by the electret. Even though the driving frequency is constant, the frequency of generator's output increases with the increase in swing

amplitude. Indeed, larger rotation angle can result in more output peaks (more travelling across) and thus higher average power (larger area under the curve).

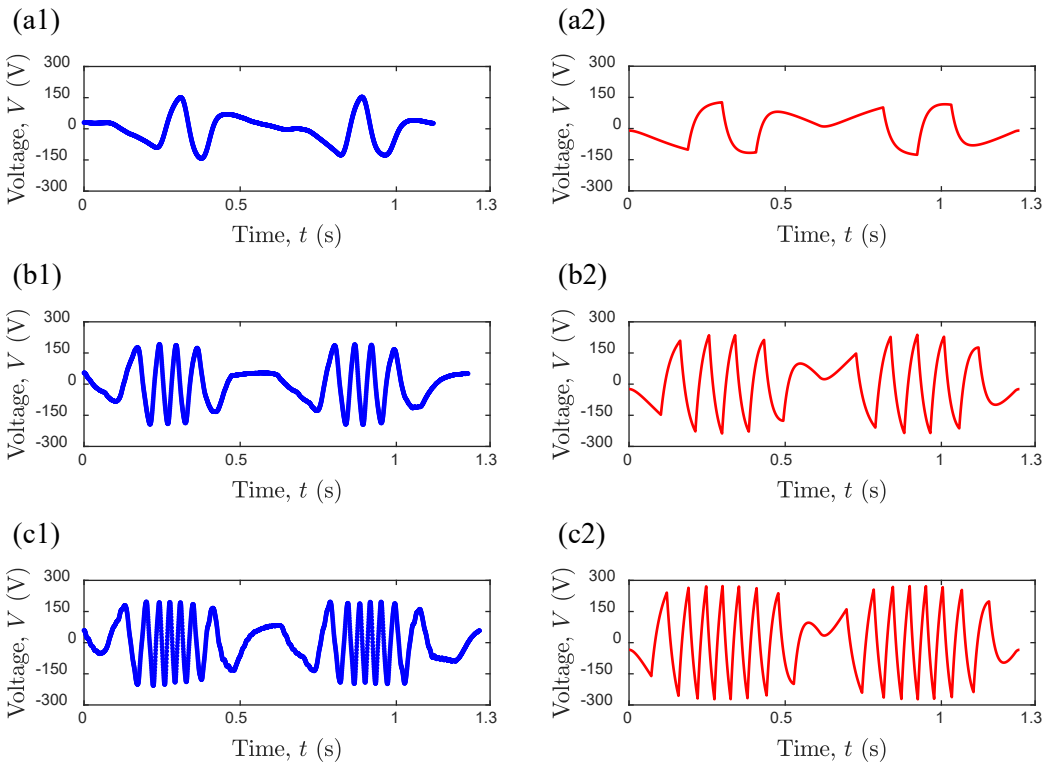

Fig. 6 Time histories (in one excitation period) of the voltage across the resistor of 80 MΩ when the generator sinusoidally swings at a frequency of 0.8 Hz under three different swing amplitudes of (a) 23.04°, (b) 57.60°, and (c) 92.16°, obtained from experiments (a1 – c1) and numerical simulations (a2 – c2), between which the overall agreement is good.

4.3. Effects of winch radius

Winch radius r_0 is one of the key parameters directly relating generator's rotation to the surge and heave of the WEC (Eq. (A1)) and determining the driving torque that is applied on the shaft by the tether tension force (Eq. (17)). The average power P_a is calculated using Eq. (21):

$$P_a = \frac{\int_0^T I^2 R \mathrm{d}t}{T} \tag{21}$$

where T is the time period adopted for evaluation. P_a varies with r_0 and maximizes at r_0 = 8.43 mm, as shown in Fig. 7(a). Correspondingly, the variations of rotation speed and peak-to-peak (P-P) rotation (or swing) amplitude with r_0 are presented in Fig. 7(b). Note that only one of the two encapsulated generators is evaluated because of their equivalence, i.e., the average power herein is of one generator or half WEC.

Obviously, the peak of the average power coincides with that of the rotation speed, rather than that of the P-P rotation amplitude, in terms of the horizontal axis or the winch radius. Therefore, rotation speed can be more dominant than rotation amplitude in contributing to the power generation, which may be explained by Eq. (19), i.e., the source current I_s is linearly proportional to the rotation speed $\dot{\theta}$. The magnitudes of the parameters used here and in the following study, if not otherwise specified, are listed in Table 1.

Table 1 Values of parameters used in this study (if not otherwise specified).

Parameter	**Value**
Mass of the WEC, m_b	0.573 kg
Radius of the WEC, R_b	7.5 cm
Moment of inertia of generators, J	1.14×10^{-4} kg m^{-2}
Damping coefficient of generators, c	3×10^{-4} J s rad^{-1}
Stiffness of torsion springs, k_s	5×10^{-3} N m rad^{-1}
Number of teeth of each electrode, n	15
Inner radius of electret, r_1	13.5 mm
Outer radius of electret, r_2	56 mm
Surface charge density, σ	36.16 μC m^{-2}
Capacitance between electrodes, C	277 pF
Load resistance, R	20 MΩ
Water depth, h; Tether length, L	0.45 m
Added mass coefficient, C_a	0.5
Drag coefficient, C_d	0.3
Wave amplitude, A	4 cm
Wave frequency, $\Omega/2\pi$	0.5 Hz

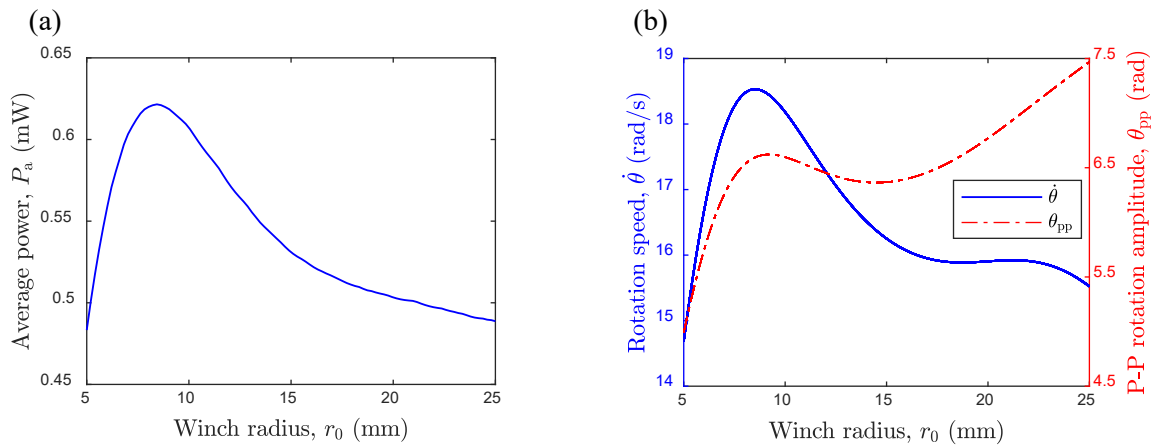

Fig. 7 Average power at different winch radii (a) and the corresponding rotation speed and P-P rotation amplitude of the generator (b). The peak of the average power coincides with that of the rotation speed, rather than that of the P-P rotation amplitude, in terms of the horizontal axis or the winch radius.

Coupling the oscillation of the WEC and the rotation of the generator, time histories of their translational (surge and heave) and rotational (rotation angle) displacements at r_0 = 8.43 mm are shown in Fig. 8(a), and the corresponding frequency spectra are given in Fig. 8(b). Clearly, the surge of the WEC is close to a simple harmonic motion with the same frequency as that of the wave excitation, while heave and rotation angle have similar frequency components among which the superharmonic 2Ω is dominant. This is because the coupling between heave and rotation is stronger than that between surge and rotation. As indicated by Eq. (A1), the longer mooring tether leads to the stronger coupling between surge and rotation. Therefore, the energy conversion performance of the WEC is closely related to its heave.

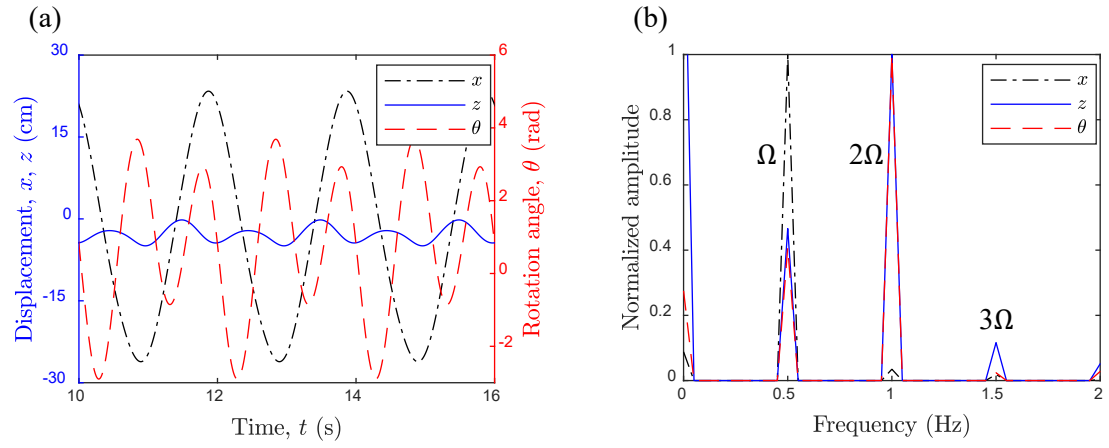

Fig. 8 Time histories (in 3 excitation periods) of the surge and heave of the WEC and the corresponding rotation angle of the generator (a), and their frequency spectra (b) at r_0 = 8.43 mm. Superharmonic components only appear in heave and rotation.

4.4. Effects of spring stiffness

The restoring torque is crucial for maintaining the oscillatory rotation of the generator. Both linear and nonlinear (cubic) torsion springs are considered, and the latter includes nonlinear softening and hardening cases. The linear restoring torque has been involved in Eq. (17), i.e., the term $k_s\theta$. Let $k_n > 0$ be the nonlinear spring stiffness, which is related to the linear one by $k_s/k_n = \alpha$, then the restoring torques of nonlinear softening and hardening torsion springs are $k_s\theta - k_n\theta^3$ and $k_s\theta + k_n\theta^3$, respectively.

These three torsion springs are compared for their restoring torques first. As shown in Fig. 9(a) (α = 100), the softening nonlinearity bends down the restoring torque curve from the linear one, while the hardening nonlinearity bends it up. The corresponding average power is compared in Fig. 9(b). It seems that the stiffness nonlinearity is not apparently beneficial to performance enhancement, though the hardening nonlinearity leads to a slightly higher peak. Hence, only the linear torsion spring will be used in the following study.

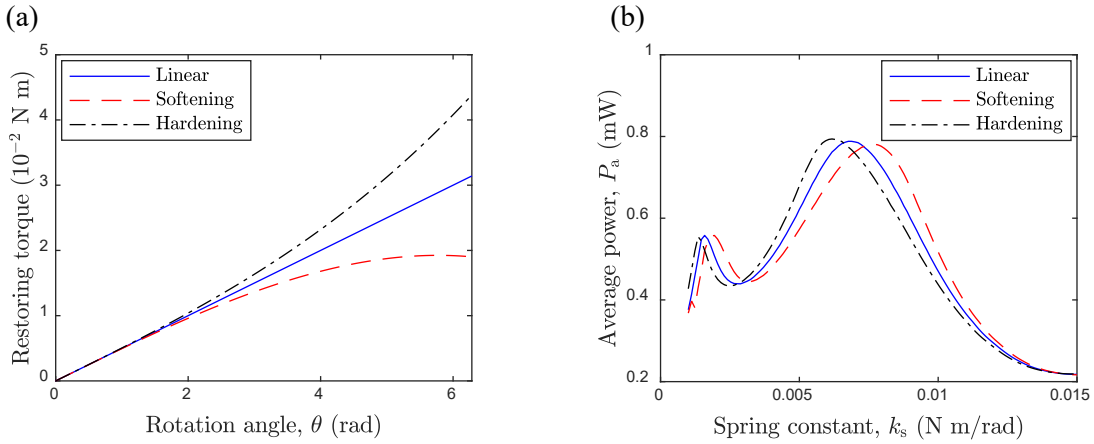

Fig. 9 Comparisons of linear and nonlinear (softening and hardening) torsion springs in terms of (a) the restoring torque provided and (b) the average power resulted. Nonlinear stiffness results in minor discrepancy on the performance, compared with the linear one.

Fig. 9(b) shows two peaks of average power when the spring constant k_s increases and their magnitude difference is significant. To look into the details, time histories (in one excitation period) of the instantaneous power and the rotation angle at these two peaks, i.e., k_s = 1.59×10^{-3} N m rad^{-1} (lower peak) and 6.77×10^{-3} N m rad^{-1} (higher peak), of the linear case are compared in Fig. 10. It can be observed that the rotation angle experiences superharmonic (2Ω) oscillation at the higher peak and approximately simple harmonic motion at the lower peak. Moreover, the superharmonic oscillation induces two additional pulse trains (clustered peaks, each pulse corresponds to a travelling across of the electret), which then results in higher average power. Besides, the dense pulse trains of the instantaneous power indicates that the low-

frequency oscillation of the WEC (or the oscillatory rotation of the generator) has been converted into electrical outputs of much higher frequencies, which will be further studied when it comes to the effect of tooth number.

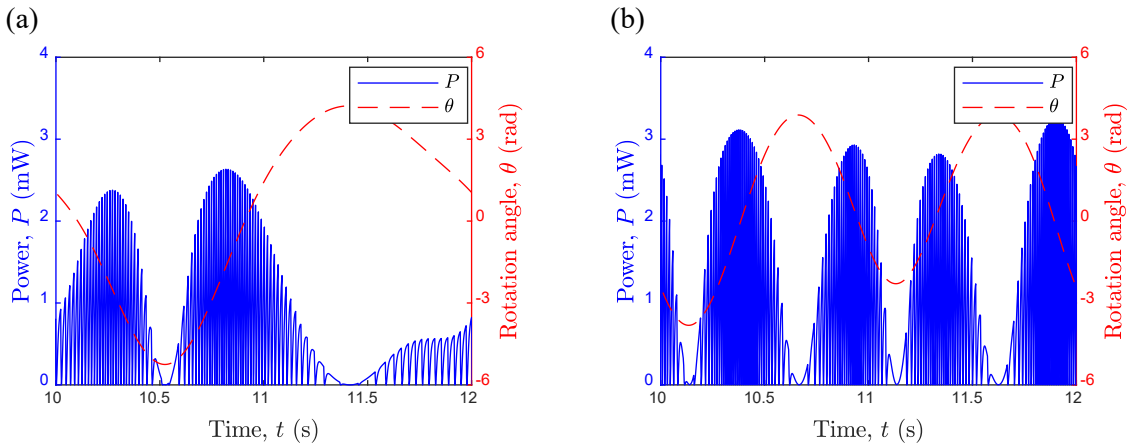

Fig. 10 Time histories (in one excitation period) of the instantaneous power and the rotation angle at the two peaks of the linear case in Fig. 9(b): (a) k_s = 1.59×10^{-3} N m rad^{-1} and (b) k_s = 6.77×10^{-3} N m rad^{-1}. The power output is in the form of pulse trains, and the superharmonic oscillation at the higher peak leads to more pulse trains and thus better performance.

4.5. Effects of wave frequency

Ocean surface gravity waves, driven by wind and restored by gravity, are the most common form of wave motions occurring at the interface between air and oceans [53], and their frequencies range from 0.033 Hz to 1 Hz [54] among which the practical WEC, therefore, should operate.

The average power at different wave frequencies is shown in Fig. 11(a), where the frequency range concerned, i.e., 0.10 – 0.75 Hz, is well covered by that of the ocean surface gravity waves. Fig. 11(b) presents the corresponding bifurcation diagram of rotation angle, where the inset is a local view of the range between 0.25 Hz and 0.3 Hz. Apparently, both the average power and the rotation angle reach their peak values at 0.61 Hz, and the peak of the former is around 1 mW. At frequencies below 0.4 Hz, the average power remains at a much lower level, and the oscillatory rotation of the generator is complicated, such as the period-doubling bifurcations (including period-3 to period-6 around 0.275 Hz, period-4 to period 8 around 0.294 Hz, etc.) shown in the inset in Fig. 11(b) and the chaotic oscillation at 0.268 Hz as shown in the phase plot (with Poincaré map represented by red circles showing the pattern of a chaotic attractor) and the frequency spectrum of θ in the left subfigures.

It is found that the oscillatory rotation of the generator experiences superharmonic resonance of order 2 at the peak frequency $\Omega/2\pi \approx 0.61$ Hz, i.e., $\omega_\theta/\Omega \approx 2$, where $\omega_\theta = \sqrt{k_s/J}$ is the undamped natural frequency, and its phase plot (with Poincaré map) and frequency spectrum are shown in the right subfigures in Fig. 11(b). In comparison with that of the chaotic oscillation at 0.268 Hz (or other oscillations at low frequencies), the oscillation at the superharmonic resonance frequency is in an orbit of much higher energy, which results in superior energy conversion performance. Therefore, one may adjust the parameters of the generator system, such as the spring constant k_s, to shift the superharmonic resonance peak towards the designated driving frequency for enhancing WEC's performance.

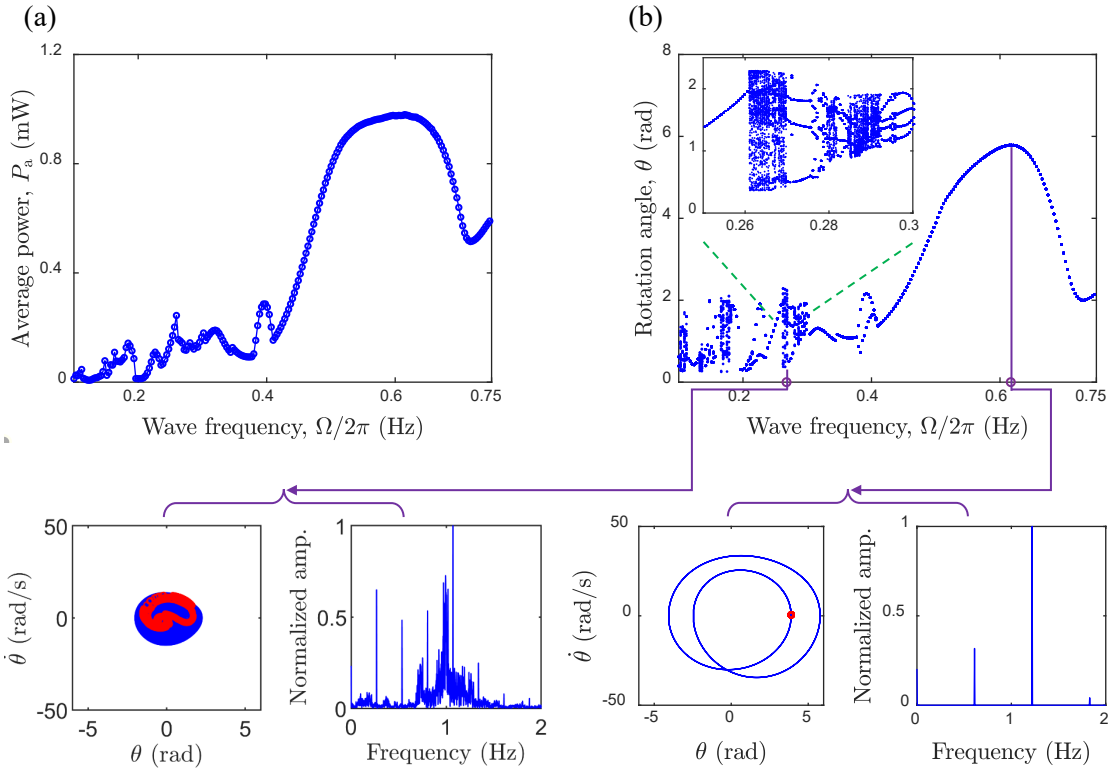

Fig. 11 Dynamic responses of the WEC: (a) Average power at different wave frequencies and (b) the corresponding bifurcation diagram of the rotation angle with subfigures showing phase plots (Poincaré maps shown in red circles) and frequency spectra at $\Omega/2\pi = 0.268$ Hz (left) and $\Omega/2\pi = 0.61$ Hz (right). Superharmonic resonance appears at $\Omega/2\pi = 0.61$ Hz and enhances the power output.

4.6. Effects of wave amplitude

For a linear undamped system, even an excitation of very small amplitude can cause large-amplitude vibration or resonance as long as its frequency coincides with the natural frequency of the system. Thus, it will be interesting to see how the wave amplitude influences WEC's performance at the superharmonic resonance frequency. The average power at different wave amplitudes when $\Omega/2\pi = 0.61$ Hz is shown in

Fig. 12. Note that the KC number, corresponding to the range of wave amplitudes considered, varies between 0.42 and 3.35, among which the use of Morison's equation should be adequate. The power obviously increases with the increase in wave amplitude. However, there is a jump or an abrupt change occurred when $A \cong 2$ cm, which leads to a significant increase of average power after the jump. Thus, even at the superharmonic resonance frequency, a certain magnitude of excitation is still required for achieving a good performance. If we regard an effective wave amplitude as the one that can result in superharmonic resonance, then, from Fig. 2, the effective wave amplitude should be larger than approximately one quarter of the radius of the WEC based on the proposed design.

More details related to the jump are revealed using phase plots (with Poincaré map shown in red circle) and frequency spectra, and those of a point (A = 1.9 cm) before the jump are shown in the left subfigures in Fig. 12, while those of the amplitude (A = 2.1 cm) after the jump are shown in the right subfigures. It is noted that the driving frequency is dominant in the frequency spectrum before the jump despite the existence of the superharmonic component 2Ω. However, it is completely reversed after the jump, i.e., 2Ω takes the dominance and induces the superharmonic resonance. The wave amplitude, at which the jump or the superharmonic resonance takes place, may then be named as the effective wave amplitude. Thus, the WEC should be designed to work above the effective wave amplitude.

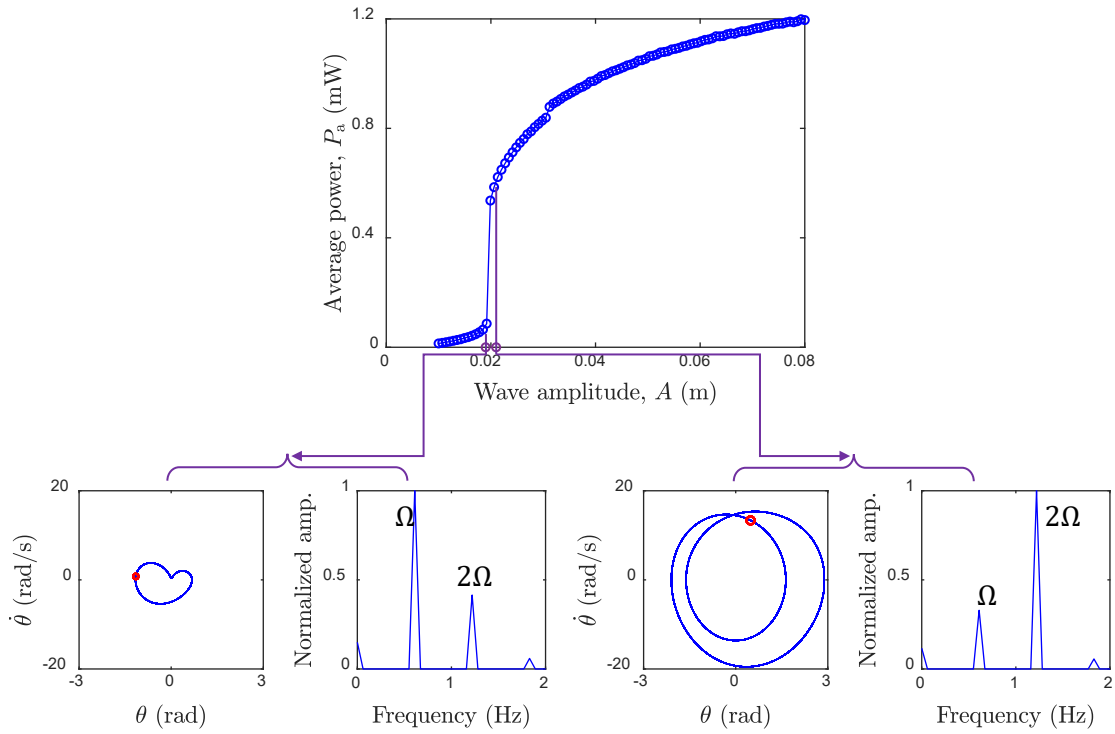

Fig. 12 Average power at different wave amplitudes when $\Omega/2\pi$ = 0.61 Hz and the phase plots (with Poincaré maps shown in red circles) and frequency spectra at A = 1.9 cm (left) and A = 2.1 cm (right). A sudden jump happens around A = 2.0 cm, after which the superharmonic component takes the dominance.

4.7. Effects of tooth number

The capacitance of the generator can be either dependent or independent on the tooth number of the comb-like electrodes, corresponding to a constant or a varying gap spacing between electrode teeth, respectively. Although the former case is more practical from the perspectives of fabrication, both of them will be studied here. For the variable-capacitance case, the total capacitance can be approximated by [55]:

$$C = \frac{2n\varepsilon_0\varepsilon_r b(r_2 - r_1)}{d} = Qn \tag{22}$$

where ε_0 is the permittivity of free space, ε_r is the dielectric constant of the media between electrodes, and b and d are the thickness of and the gap spacing between electrode teeth, respectively. Apparently, the capacitance is linearly proportional to the tooth number with a coefficient Q which can be determined using the measured C (277 pF) at n = 15. For the constant-capacitance case, C = 277 pF is adopted for different tooth numbers.

The average power at different tooth numbers in both cases are shown in Fig. 13. Clearly, there exists a peak in the variable-capacitance case, whereas the relationship between variables is positive monotonic in the constant-capacitance case. The peak average power is about 2 mW at n = 8 under the wave excitation of the superharmonic frequency 0.61 Hz. Excitation frequencies around the superharmonic resonance result in similar optimal tooth numbers, despite that their corresponding average power is lower. In the second case, the nonlinear monotonicity leads to a gradual increase in average power which seems to reach a steady value eventually.

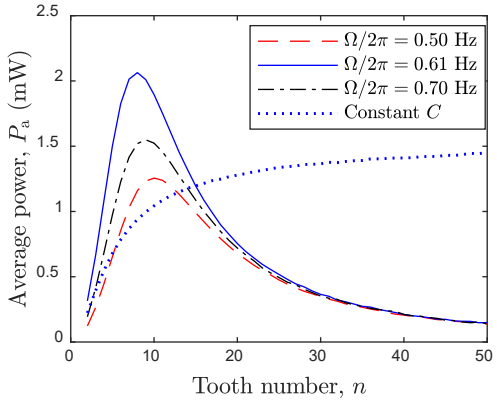

Fig. 13 Average power at different tooth numbers in both cases of variable (under the wave excitation of the same amplitude A = 8 cm but three different frequencies including the superharmonic resonance frequency 0.61 Hz) and constant capacitance (under the wave excitation of A = 8 cm and $\Omega/2\pi$ = 0.61 Hz). Optimal value exists in the former case, while the latter case results in monotonical variation.

In fact, the teeth of the two groups of comb-like electrodes are staggered, and every two neighboring teeth compose a pair. A pulse will be generated when the electret travels across such a pair. Thus, the tooth number determines the frequency of electrical outputs, and the larger the tooth number, the higher the frequency, which is demonstrated in Fig. 14, where the spectrograms (the frequency response is time-variant) of the current outputs at n = 8 and n = 40 in the second case are compared. The difference is significant, and the highest dominant frequency is around 70 Hz at n = 8, while it is more than quadrupled (around 310 Hz) at n = 40. Such high frequency or large tooth number results in higher average power when the capacitance is independent of the tooth number, while a trade-off between these two parameters, i.e., n and C, is achieved at the peak if they are related. The following study will use n = 8 that corresponds to the peak in the variable-capacitance case.

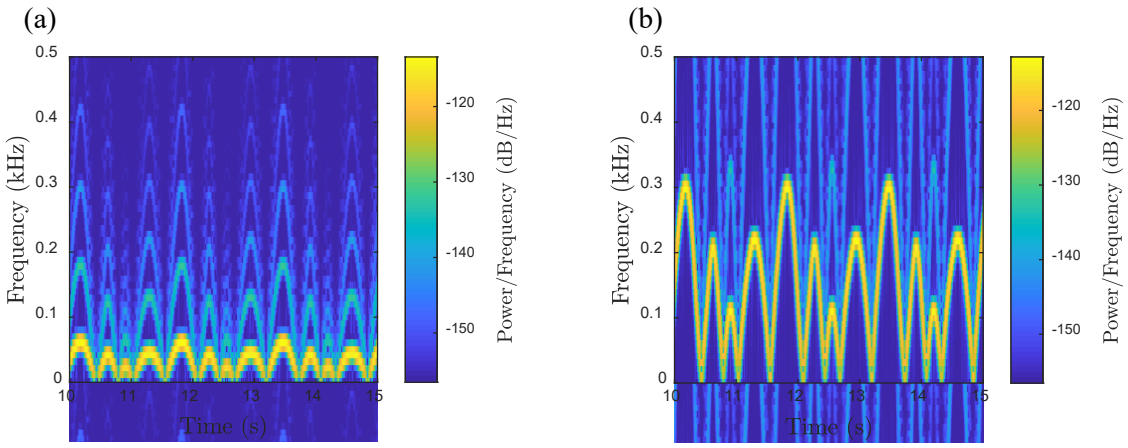

Fig. 14 Spectrograms of the current outputs at (a) n = 8 and (b) n = 40 in the constant-capacitance case. The frequency of the WEC's electrical output can be much higher than that of the wave excitation and is dependent on the tooth number of the comb-like electrodes.

4.8. Effects of load resistance

The internal impedance of electrostatic energy converters is usually quite high, and so is the matched load resistance. The average power and root-mean-square (RMS) voltage are obtained at different load resistances under the wave excitation (A = 8 cm) of three different frequencies, and they are shown in Fig. 15(a) and (b), respectively. The matched load resistance is 20 MΩ at 0.61 Hz, corresponding to a peak average power of around 2 mW, and other wave frequencies near 0.61 Hz have similar matching values.

Fig. 15(b) suggests that the open-circuit voltage is around 300 V, which is in accordance with the characteristics of electrostatic energy converters, i.e., high open-circuit voltage and low short-circuit current.

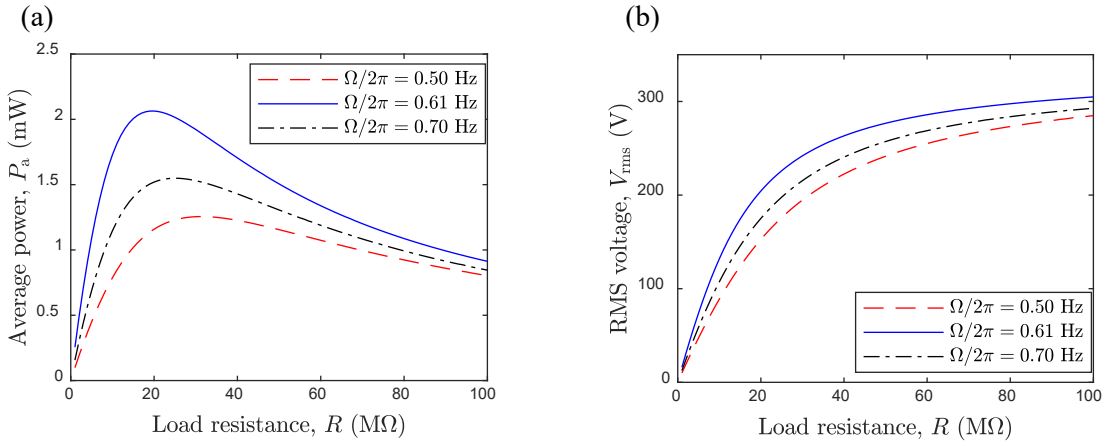

Fig. 15 Average power (a) and RMS voltage (b) at different load resistances under the wave excitation of three different frequencies. The matched load resistance and the open-circuit voltage at superharmonic resonance is around 20 MΩ and 300 V, respectively.

4.9. Irregular wave excitation

The JONSWAP spectrum is a common representation of irregular surface waves in the frequency domain and is developed based on the field observations in the North Sea [56,57]. The spectrum is expressed as:

$$S(\Omega_i) = \frac{5}{16} H_{sw}^2 \frac{\Omega_p^4}{\Omega_i^5} \exp\left[-\frac{5}{4}\left(\frac{\Omega_i}{\Omega_p}\right)^{-4}\right] \gamma^{\exp\left[-\frac{1}{2\mu^2}\left(\frac{\Omega_i}{\Omega_p}-1\right)^2\right]} \tag{23}$$

where Ω_i denotes the i-th wave frequency, H_{sw} is the significant wave height, Ω_p is the peak frequency, γ is the shape parameter and equals 3.3, and μ takes one of the following two values:

$$\mu = \begin{cases} 0.07, & \Omega_i \le \Omega_p \\ 0.09, & \Omega_i > \Omega_p \end{cases}$$

The amplitude of the i-th wave component is given by:

$$A_i = \sqrt{2S(\Omega_i)\Delta\Omega} \tag{24}$$

where the frequency interval $\Delta\Omega = \frac{\Omega_u - \Omega_l}{N}$ with Ω_l and Ω_u being the lower and upper limits of Ω_i, respectively.

Hence, the horizontal and vertical velocities of the fluid particles in irregular waves are:

$$u(x,z,t) = \sum_{i=1}^{N} A_i \Omega_i \frac{\cosh[k_i(z+h)]}{\sinh(k_i h)} \cos(\Omega_i t - k_i x + \varphi_i) \tag{25}$$

$$v(x,z,t) = \sum_{i=1}^{N} -A_i \Omega_i \frac{\sinh[k_i(z+h)]}{\sinh(k_i h)} \sin(\Omega_i t - k_i x + \varphi_i) \tag{26}$$

where φ_i are random phase angles between 0 and 2π, and the related accelerations can be derived accordingly. Thus, the forces exerted on the WEC by irregular wave loadings can be obtained by substituting Eqs. (23 – 26) into Eqs. (5) and (6).

An example of the JONSWAP spectrum ($\Omega_p/2\pi$ = 0.4 Hz, H_{sw} = 5 cm) is shown in Fig. 16(a) and (b) in terms of its wave spectral density distribution and time-domain realization, respectively. It is noted that the spectral density distribution is asymmetric about the peak frequency because of μ, a step function of wave frequency.

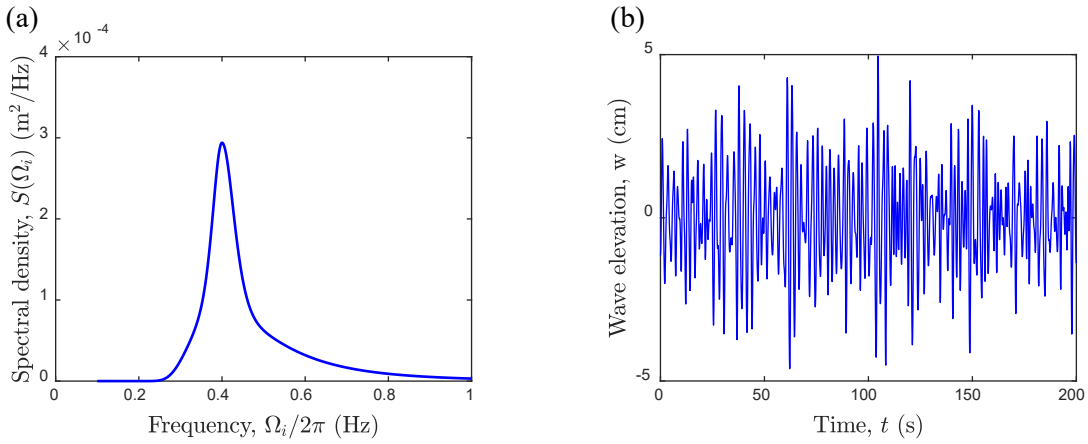

Fig. 16 Wave spectral density distribution of a JONSWAP spectrum (a) and its time-domain realization in terms of wave elevation (b). The peak frequency and the significant wave height are $\Omega_p/2\pi$ = 0.4 Hz and H_{sw} = 5 cm, respectively.

The effects of peak frequency and significant wave height on average power are demonstrated in Fig. 17, where the straight lines are linear fittings. Approximately, average power varies linearly against both peak frequency and significant wave height, especially against the latter, which intrinsically differs from the variation of average power against the frequency and amplitude of a monochromatic wave. Besides, it seems that no superharmonic resonance emerges around $\Omega_p/2\pi$ = 0.6 Hz, which is due to the variable excitation frequency despite that it has peak spectral density at 0.6 Hz. Nevertheless, such linearity may be

favorable in predicting the power output of a wave farm if the proposed WECs are deployed. Note that T = 500 s is used to evaluate the average power, considering that a longer time period or more samples can reduce the error incurred by averaging.

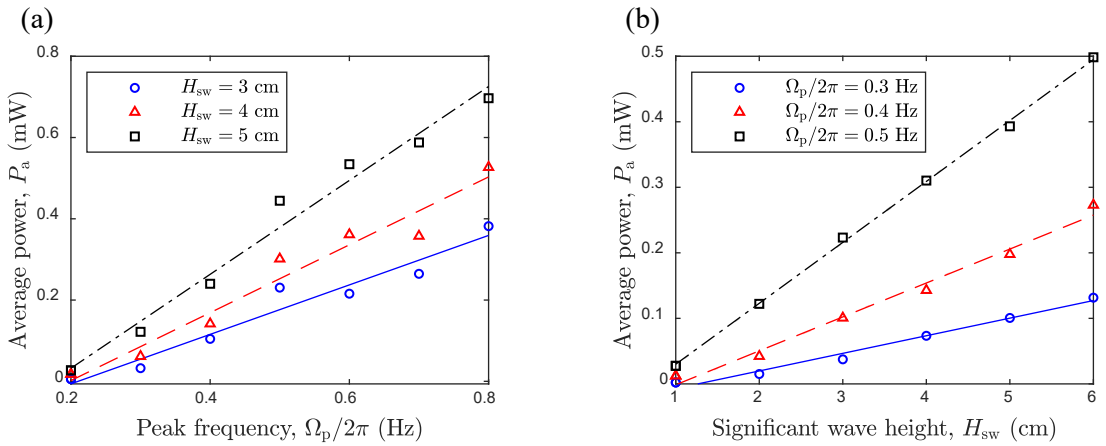

Fig. 17 Diagrams of average power versus peak frequency (a) and significant wave heights (b). The average power varies approximately linearly against both peak frequency and significant wave height.

5. Concluding remarks

This paper proposes a dynamical model for an electret-based wave energy converter (WEC) and presents the parametric analysis of the electromechanical system. The proposed spherical WEC is taut-moored by a single tether and incorporates electret-based rotational generators as the PTO system, which is distinct from that of the conventional WECs, for electrostatic energy conversion. Linear wave theory and Morison equation are applied for wave field and forces, respectively. Only surge and heave motions of the WEC are considered, and they are coupled with the rotation of generators. The electrical system of the generator is equivalent to a current source and a capacitor, forming a parallel RC circuit when connected to a load resistance. The governing equations of the nonlinear and non-smooth electromechanical system are solved using event-driven algorithms developed with the MATLAB built-in function *events* and solver *ode15s*.

Good agreement between experimental and numerical results of generator's output demonstrates the validity of the theoretical model for the electret-based rotational generator. Effects of some key parameters on the performance of the WEC under regular/sinusoidal wave excitation are then investigated numerically. Firstly, the influences of two parameters related to the mechanical system of the WEC, i.e., winch radius and spring stiffness, are studied. The average power is found to be more dependent on oscillatory rotation speed rather than amplitude, which is believed to be due to the fact the current source is proportional to the rotation speed, giving rise to an optimal winch radius at which both the speed and the power reach their maxima. It has been demonstrated that nonlinear stiffness is beneficial to some vibration energy harvesters

[58,59]. However, in our system, the torsion spring involving stiffness hardening or softening makes minor difference compared to the linear one, suggesting the adoption of linear elastic response.

Then, that of the wave parameters, including wave frequency and amplitude, is analysed. Superharmonic resonance can be used to enhance the energy conversion performance at relatively low frequencies, though its occurrence requires wave excitation of certain amplitude which should be larger than approximately one quarter of the radius of the WEC. Additionally, for irregular waves with the JONSWAP spectrum, average power varies linearly with both the peak frequency and the significant wave height, which intrinsically differs from the case of sinusoidal wave excitation, but such linear relationships may be useful for prediction and optimization when the WECs are to be tested in open water.

Lastly, that of the electrical parameters, i.e., electrode tooth number and load resistance, is investigated. The tooth number of the comb-like electrodes determines the frequencies of electrical outputs, i.e., larger tooth number leads to higher frequencies (up to hundreds of Hz), but an optimal value can be found when tooth number and generator's capacitance are relevant. Besides, at superharmonic resonance, a matched load resistance of 20 MΩ results in a peak average power of around 2 mW from one of the two generators encapsulated in the WEC of a diameter of 15 cm, and more generator modules (serial assembly of generators with stepped diameters) can be accommodated for enhanced performance.

The findings shed light on the characteristics of electret-based WECs. It should be noted that the proposed theoretical model has been partially used to describe our WEC prototype and agreed with the preliminary test results (see details in [33]). However, the optimized WEC after the parametric study described in this work still requires a thorough experimental validation, which will be carried out as a future work. Besides, considering that the average power output of the electret-based rotational generator is proportional to generator's diameter to the power of 4 [33], scale-up models of the electret-based WEC are promising for practical applications. The corresponding scale-up method is then worth studying as well.

Acknowledgements

This work was supported by the NSFC/RGC Joint Research Scheme (N_PolyU519/19) and the Postdoctoral matching fund of HKPolyU (P0034926).

Appendix

The above mechanical and electrical systems are coupled. Particularly, the rotation of generators is coupled with the surge and heave of the WEC, which will cancel out the rotation angle θ and its derivatives and leave five independent state variables, namely x, $\dot{x}$, z, $\dot{z}$, and I.

The relation between the rotation angle of generators and the extension of the tether is:

$$\theta = \frac{\Delta L}{r_0} = \frac{\sqrt{(L+z)^2 + x^2} - L}{r_0} \tag{A1}$$

By setting $\boldsymbol{q} = [q_1, q_2, q_3, q_4, q_5\,]^{\mathrm{T}} = [x, \dot{x}, z, \dot{z}, I]^{\mathrm{T}}$ and combining the above equations, the governing equations of the WEC system can be rewritten as:

$$\boldsymbol{M}(t, \boldsymbol{q})\dot{\boldsymbol{q}} = \boldsymbol{F}(t, \boldsymbol{q}) \tag{A2}$$

where matrix $\boldsymbol{M}(t, \boldsymbol{q})$ and $\boldsymbol{F}(t, \boldsymbol{q})$ are formed as:

$$\boldsymbol{M}(t, \boldsymbol{q}) = \begin{bmatrix} 1 & 0 & 0 & 0 & 0 \\ 0 & M_{22} & 0 & M_{24} & 0 \\ 0 & 0 & 1 & 0 & 0 \\ 0 & M_{42} & 0 & M_{44} & 0 \\ 0 & 0 & 0 & 0 & M_{55} \end{bmatrix}$$

$$\boldsymbol{F}(t, \boldsymbol{q}) = [q_2 \quad F_2 \quad q_4 \quad F_4 \quad F_5]^{\mathrm{T}}$$

with the symbolic components given by:

$$M_{22} = m_{\mathrm{b}} + \rho V_{\mathrm{s}} C_{\mathrm{a}} + \frac{J}{K} q_1 \sin\alpha, M_{24} = \frac{J}{K}(L + q_3)\sin\alpha$$

$$M_{42} = \frac{J}{K} q_1 \cos\alpha, M_{44} = m_{\mathrm{b}} + \rho V_{\mathrm{s}} C_{\mathrm{a}} + \frac{J}{K}(L + q_3)\cos\alpha, M_{55} = RC$$

$$F_2 = \rho V_{\mathrm{s}} C_{\mathrm{m}} \dot{u} + \frac{1}{2}\rho C_{\mathrm{d}} A_{\mathrm{p}x}(u - q_2)^2 \mathrm{sgn}(u - q_2) - G_1 \sin\alpha - G_2 \frac{J}{K}\sin\alpha$$

$$F_4 = \rho V_{\mathrm{s}} C_{\mathrm{m}} \dot{v} + \frac{1}{2}\rho C_{\mathrm{d}} A_{\mathrm{p}z}(v - q_4)^2 \mathrm{sgn}(v - q_4) - G_1 \cos\alpha - G_2 \frac{J}{K}\cos\alpha + F_{\mathrm{b}}$$

$$F_5 = \frac{r_0 n \sigma \delta}{2K}(r_2^2 - r_1^2)[(L + q_3)q_4 + q_1 q_2] - q_5$$

$$K = r_0^2 \sqrt{(L + q_3)^2 + q_1^2}$$

$$G_1 = \frac{c}{K}[(L + q_3)q_4 + q_1 q_2] + \frac{k_{\mathrm{s}}}{r_0^4}(K - r_0^2 L) + F_{\mathrm{p}}$$

$$G_2 = (q_2^2 + q_4^2) - \frac{r_0^4}{K^2}[(L + q_3)q_4 + q_1 q_2]^2$$

References:

[1] Barstow S, Mørk G, Mollison D, Cruz J. The wave energy resource. Ocean wave energy, Springer; 2008, p. 93–132.

[2] Enerdata. World Energy & Climate Statistics – Yearbook 2022. 2022.

[3] Salter SH. Wave power. Nature 1974;249:720–4.

[4] Drew B, Plummer AR, Sahinkaya MN. A review of wave energy converter technology 2009.

[5] Bosserelle C, Reddy S, Krüger J. Cost analysis of wave energy in the Pacific. Waves and Coasts in the Pacific 2015.

[6] Christensen L, Friis-Madsen E, Kofoed JP, Tedd J. Worlds largest wave energy project 2007 in Wales. Proc. POWER-GEN 2006 Eur. Conf. Col. Ger. June 2006, 2006.

[7] Rusu E, Onea F. A review of the technologies for wave energy extraction. Clean Energy 2018;2:10–9.

[8] Wang ZL. Catch wave power in floating nets. Nature 2017;542:159–60.

[9] Wang ZL, Jiang T, Xu L. Toward the blue energy dream by triboelectric nanogenerator networks. Nano Energy 2017;39:9–23. https://doi.org/10.1016/j.nanoen.2017.06.035.

[10] Seol M-L, Lee S-H, Han J-W, Kim D, Cho G-H, Choi Y-K. Impact of contact pressure on output voltage of triboelectric nanogenerator based on deformation of interfacial structures. Nano Energy 2015;17:63–71.

[11] Xu W, Wong M-C, Hao J. Strategies and progress on improving robustness and reliability of triboelectric nanogenerators. Nano Energy 2019;55:203–15.

[12] Li X, Wang Y, Xu M, Shi Y, Wang H, Yang X, et al. Polymer electrets and their applications. J Appl Polym Sci 2021;138:50406.

[13] Mellouki H, Herous L, Prawatya Y, Neagoe B, Dascalescu L. Tribo and corona charging and charge decay on polymers plates. 2017 5th Int. Conf. Electr. Eng., IEEE; 2017, p. 1–5.

[14] Miyoshi T, Adachi M, Suzuki K, Liu Y, Suzuki Y. Low-profile rotational electret generator using print circuit board for energy harvesting from arm swing. 2018 IEEE Micro Electro Mech. Syst., IEEE; 2018, p. 230–2.

[15] Boisseau S, Despesse G, Sylvestre A. Optimization of an electret-based energy harvester. Smart Mater Struct 2010;19:75015.

[16] Wada N, Horiuchi N, Mukougawa K, Nozaki K, Nakamura M, Nagai A, et al. Electrostatic induction power generator using hydroxyapatite ceramic electrets. Mater Res Bull 2016;74:50–6.

[17] Bi M, Wang S, Wang X, Ye X. Freestanding-electret rotary generator at an average conversion efficiency of 56%: theoretical and experimental studies. Nano Energy 2017;41:434–42.

[18] Cheng P, Guo H, Wen Z, Zhang C, Yin X, Li X, et al. Largely enhanced triboelectric nanogenerator for efficient harvesting of water wave energy by soft contacted structure. Nano Energy 2019;57:432–9.

[19] Liang X, Jiang T, Liu G, Feng Y, Zhang C, Wang ZL. Spherical triboelectric nanogenerator

integrated with power management module for harvesting multidirectional water wave energy. Energy Environ Sci 2020;13:277–85.

[20] Jusoh MA, Ibrahim MZ, Daud MZ, Albani A, Mohd Yusop Z. Hydraulic power take-off concepts for wave energy conversion system: A review. Energies 2019;12:4510.

[21] Zhang H, Zhang J, Zhou X, Shi Q, Xu D, Sun Z, et al. Robust performance improvement of a raft-type wave energy converter using a nonlinear stiffness mechanism. Int J Mech Sci 2021;211:106776.

[22] Liermann M, Samhoury O, Atshan S. Energy efficiency of pneumatic power take-off for wave energy converter. Int J Mar Energy 2016;13:62–79.

[23] Li M, Wu R, Wu B, Yang Z, Li G. Hydrodynamic performance and optimization of a pneumatic type spar buoy wave energy converter. Ocean Eng 2022;254:111334.

[24] Khatri P, Wang X. Comprehensive review of a linear electrical generator for ocean wave energy conversion. IET Renew Power Gener 2020;14:949–58.

[25] Sun R, Wong W, Cheng L. Hybrid electromagnetic shunt damper with Coulomb friction and negative impedance converter. Int J Mech Sci 2022;230:107552.

[26] Meng F, Ding B, Cazzolato B, Arjomandi M. Modal analysis of a submerged spherical point absorber with asymmetric mass distribution. Renew Energy 2019;130:223–37.

[27] Orszaghova J, Wolgamot H, Draper S, Eatock Taylor R, Taylor PH, Rafiee and A. Transverse motion instability of a submerged moored buoy. Proc R Soc A 2019;475:20180459.

[28] Orszaghova J, Wolgamot H, Draper S, Taylor PH, Rafiee A. Onset and limiting amplitude of yaw instability of a submerged three-tethered buoy. Proc R Soc A 2020;476:20190762.

[29] Bailey H, Bryden IG. Influence of a quadratic power take-off on the behaviour of a self-contained inertial referenced wave energy converter. Proc Inst Mech Eng Part M J Eng Marit Environ 2012;226:15–22.

[30] Bailey H. Influence of a nonlinear power take off on a wave energy converter. Ph D Diss PhD Thesis 2010.

[31] Zhang X, Yang J. Power capture performance of an oscillating-body WEC with nonlinear snap through PTO systems in irregular waves. Appl Ocean Res 2015;52:261–73.

[32] Giassi M, Thomas S, Tosdevin T, Engström J, Hann M, Isberg J, et al. Capturing the experimental behaviour of a point-absorber WEC by simplified numerical models. J Fluids Struct 2020;99:103143.

[33] Fu Y, Ruan H. Experimental and theoretical investigations of a novel electret-based wave energy converter. Nano Energy n.d. https://doi.org/10.1016/j.nanoen.2022.107854.

[34] Ogihara K. Theoretical analysis on the transverse motion of a buoy by surface wave. Appl Ocean Res 1980;2:51–6.

[35] Williamson CHK, Govardhan R. Dynamics and forcing of a tethered sphere in a fluid flow. J Fluids Struct 1997;11:293–305.

[36] Radhakrishnan S, Datla R, Hires RI. Theoretical and experimental analysis of tethered buoy instability in gravity waves. Ocean Eng 2007;34:261–74.

[37] Craik ADD. The origins of water wave theory. Annu Rev Fluid Mech 2004;36:1–28.

[38] Finnegan W, Goggins J. Numerical simulation of linear water waves and wave–structure interaction. Ocean Eng 2012;43:23–31.

[39] Penalba M, Giorgi G, Ringwood J V. Mathematical modelling of wave energy converters: A review

of nonlinear approaches. Renew Sustain Energy Rev 2017;78:1188–207.

[40] Morison JR, Johnson JW, Schaaf SA. The force exerted by surface waves on piles. J Pet Technol 1950;2:149–54.

[41] Keulegan GH, Carpenter LH. Forces on cylinders and plates in an oscillating fluid. J Res Natl Bur Stand (1934) 1958;60:423–40.

[42] Boisseau S, Despesse G, Seddik BA. Electrostatic conversion for vibration energy harvesting. Small-Scale Energy Harvest 2012;5.

[43] Longuet-Higgins MS. Mass transport in water waves. Philos Trans R Soc London Ser A, Math Phys Sci 1953;245:535–81.

[44] Ballard Z, Mann BP. Two-dimensional nonlinear analysis of an untethered spherical buoy due to wave loading. J Comput Nonlinear Dyn 2013;8.

[45] Fredsoe J, Sumer BM. Hydrodynamics around cylindrical structures (revised edition). vol. 26. World Scientific; 2006.

[46] Milne-Thomson LM. Theoretical hydrodynamics. Courier Corporation; 1996.

[47] Qin H, Gu G, Shang W, Luo H, Zhang W, Cui P, et al. A universal and passive power management circuit with high efficiency for pulsed triboelectric nanogenerator. Nano Energy 2020;68:104372.

[48] Harmon W, Bamgboje D, Guo H, Hu T, Wang ZL. Self-driven power management system for triboelectric nanogenerators. Nano Energy 2020;71:104642.

[49] Liu W, Wang Z, Wang G, Zeng Q, He W, Liu L, et al. Switched-capacitor-convertors based on fractal design for output power management of triboelectric nanogenerator. Nat Commun 2020;11:1–10.

[50] Zhang H, Marty F, Xia X, Zi Y, Bourouina T, Galayko D, et al. Employing a MEMS plasma switch for conditioning high-voltage kinetic energy harvesters. Nat Commun 2020;11:1–10.

[51] Wang Z, Liu W, He W, Guo H, Long L, Xi Y, et al. Ultrahigh electricity generation from low-frequency mechanical energy by efficient energy management. Joule 2021;5:441–55.

[52] Acary V, Brogliato B. Numerical methods for nonsmooth dynamical systems: applications in mechanics and electronics. Springer Science & Business Media; 2008.

[53] Uchiyama Y. Surface gravity and capillary waves. Encycl Ocean Sci 2019:672–81.

[54] Kinsman B. Wind waves: their generation and propagation on the ocean surface. Courier Corporation; 1984.

[55] Legtenberg R, Groeneveld AW, Elwenspoek M. Comb-drive actuators for large displacements. J Micromechanics Microengineering 1996;6:320.

[56] Hasselmann K, Barnett TP, Bouws E, Carlson H, Cartwright DE, Enke K, et al. Measurements of wind-wave growth and swell decay during the Joint North Sea Wave Project (JONSWAP). Ergaenzungsh Zur Dtsch Hydrogr Zeitschrift, R A 1973.

[57] Aggarwal A, Chella MA, Kamath A, Bihs H, Arntsen ØA. Irregular wave forces on a large vertical circular cylinder. Energy Procedia 2016;94:504–16.

[58] Ramlan R, Brennan MJ, Mace BR, Kovacic I. Potential benefits of a non-linear stiffness in an energy harvesting device. Nonlinear Dyn 2010;59:545–58.

[59] Fang S, Chen K, Xing J, Zhou S, Liao W-H. Tuned bistable nonlinear energy sink for simultaneously improved vibration suppression and energy harvesting. Int J Mech Sci 2021;212:106838.